



## Article

# Landslide Detection and Mapping Based on SBAS-InSAR and PS-InSAR: A Case Study in Gongjue County, Tibet, China

Jiaming Yao <sup>1,2,3</sup>, Xin Yao <sup>1,2,\*</sup> and Xinghong Liu <sup>1,2</sup>

<sup>1</sup> Key Laboratory of Active Tectonics and Geological Safety, Ministry of Natural Resources, Beijing 100081, China

<sup>2</sup> Institute of Geomechanics, Chinese Academy of Geological Sciences, Beijing 100081, China

<sup>3</sup> University of Chinese Academy of Sciences, Beijing 100049, China

\* Correspondence: yaoxin@mail.cgs.gov.cn

**Abstract:** The rock mass along the Jinsha River is relatively broken under complex geological action. Many ancient landslides were distributed along the Jinsha River in Gongjue County, which is very dangerous under the action of gravity, tectonic stress and river erosion. Efficient and accurate identification and monitoring of landslides is important for disaster monitoring and early warning. Interferometric synthetic aperture radar (InSAR) technology has been proved to be an effective technology for landslide hazard identification and mapping. However, great uncertainty inevitably exists due to the single deformation observation method, resulting in wrong judgment during the process of landslide detection. Therefore, to address the uncertainties arising from single observations, a cross-comparison method is put forward using SBAS-InSAR (small baseline subset InSAR) and PS-InSAR (permanent scatterers InSAR) technology. Comparative analysis of the spatial complementarity of interference points and temporal deformation refined the deformation characteristics and verified the reliability of the InSAR results, aiding in the comprehensive identification and further mapping of landslides. Landslides along the Jinsha River in Gongjue County were studied in this paper. Firstly, 14 landslides with a total area of 20 km<sup>2</sup> were identified by using two time-series InSAR methods. Then, the deformation characteristics of these landslides were validated by UAV (unmanned aerial vehicle) images, multiresource remote sensing data and field investigation. Further, the precipitation data were introduced to analyze the temporal deformation characteristics of two large landslides. Lastly, the influence of fault activity on landslide formation is further discussed. Our results demonstrate that the cross-comparison of the time-series InSAR method can effectively verify the accuracy of landslide identification.

**Keywords:** time-series deformation; InSAR; landslide detection; remote sensing; rainfall



**Citation:** Yao, J.; Yao, X.; Liu, X. Landslide Detection and Mapping Based on SBAS-InSAR and PS-InSAR: A Case Study in Gongjue County, Tibet, China. *Remote Sens.* **2022**, *14*, 4728. <https://doi.org/10.3390/rs14194728>

Academic Editors: Francesca Bozzano, Paolo Mazzanti and Benedetta Antonielli

Received: 9 August 2022

Accepted: 15 September 2022

Published: 21 September 2022

**Publisher's Note:** MDPI stays neutral with regard to jurisdictional claims in published maps and institutional affiliations.



**Copyright:** © 2022 by the authors. Licensee MDPI, Basel, Switzerland. This article is an open access article distributed under the terms and conditions of the Creative Commons Attribution (CC BY) license (<https://creativecommons.org/licenses/by/4.0/>).

## 1. Introduction

Owing to complex topography, intense river erosion and geological conditions in the Jinsha River basin, landslide geological hazards occur frequently. In history, many large disaster events have occurred on the upper Jinsha River, resulting in landslides and flooding disasters, such as the landslide-dammed Temi Lake (about 1.8 ka BP) and the ancient landslide Xuelongnang Lake (about 2.1 ka BP) [1–3]. In late 2018 (11 October and 3 November 2018), the Baige landslides occurred successively in Boro Town, Tibet, China, which caused upstream inundation and downstream flooding. Additionally, the flood formed after the Baige landslides revived ancient landslides downstream and accelerated the destruction process of the landslides. Identification and monitoring of these landslides is of great importance for the safety of downstream residents and major projects. Therefore, there is an urgent need to carry out effective landslide identification and deformation monitoring for disaster risk assessment and prevention [4]. As an economical and effective monitoring method, InSAR technology has been widely used in landslide identification

and deformation monitoring [5–9], and it is also of great significance for landslide-inducing factors, failure-time prediction and risk assessment [10–14].

The installation of field monitoring stations is difficult due to the steep terrain and underdeveloped traffic along the Jinsha River. In contrast, InSAR technology is more popular because it can obtain large-scale deformation information based on SAR satellite data [2]. At present, with the accumulation of free Sentinel-1 SAR data, time-series monitoring technology of landslides is further developed [15–18]. In particular, SBAS-InSAR and PS-InSAR, based on different principles, are the mainstream time-series deformation monitoring methods [19]. PS-InSAR uses highly coherent scattered points in cell resolution; in contrast, SBAS aims at exploiting the coherence of spatial distribution in short baselines. However, active landslides can be identified effectively only by obtaining accurate deformation information [20]. Without verification of ground monitoring sites, the accuracy and reliability of singular InSAR deformation monitoring are affected to a certain extent, and the possibility of erroneous judgment in landslide identification increases.

InSAR technology has been used to study ancient landslides in this area. Liu [9] calculated a long-term deformation field in the Gongjue area using multiplatform SAR images. The three-dimensional deformation field of active landslides was inverted, and inducing factors were preliminarily analyzed. Yao [10] focused on an active landslide in Gongjue County and studied the displacement characteristics in the most recent five years through multitemporal remote sensing technology and dynamic failure-trend simulation. In this area, there are many studies on landslide deformation characteristics based on InSAR technology, but there are few comparative analyses among InSAR methods. In terms of comparative analysis of time-series InSAR methods, the cross-comparison between SBAS and PS-InSAR shows that high accuracy deformation satisfies the monitoring requirements and has great potential [21]. Biswas [22] cross-compared PS-InSAR and SBAS methods using mean LOS velocity and time-series in Las Vegas, Nevada, USA, and InSAR measurements showed similar patterns. Xu [23] evaluated the applicability of PS-InSAR and SBAS methods for monitoring the Great Wall, demonstrating the potential of these methods for the health diagnosis of heritage sites. Bui [24] evaluated the relationship between groundwater depletion and surface subsidence using PS-InSAR and SBAS-InSAR methods. Moghaddam [25] applied two InSAR methodologies above coal-seam gas (CSG) mining sites. In general, the comparative analysis of two time-series InSAR methods is effective to verify deformation information. However, this method lacks quantitative comparative analysis and external data verification in the landslide application, which is also a deficiency of the current study on the quantitative deformation characteristics of landslides in the study area.

Incorrect deformation results can lead to incorrect identification of the landslide [14], and reliable deformation information is important for landslide disaster mapping. Using different InSAR methods for landslide identification and cross-validation can play an important role in reducing false positives in landslide identification and disaster mapping [9,26]. Therefore, this paper uses free Sentinel-1 SAR data as data sources and considers ancient landslides in Gongjue County as the research focus; the main content of this study was to propose a cross-complementary InSAR method to identify landslides. External DEM data and multitemporal remote sensing data help verify the accuracy of displacement information.

The following research is carried out in this paper: (1) time-series displacement monitoring in Gongjue County based on SBAS and PS-InSAR, (2) verification of landslide deformation characteristics through UAV and field investigation, and (3) landslide mechanism research. Based on two time-series InSAR methods, external UAV and field investigation, an accurate deformation field of the landslide was obtained. Then, the relationship between landslide movement and rainfall condition was analyzed based on the time-series displacement and rainfall data. Moreover, the influence of Quaternary tectonic activity on landslide formation is discussed. Our research will benefit landslide deformation characteristics

and deformation mechanism research, thereby providing relevant references for the InSAR reliability verification.

## 2. Study Area and Datasets

### 2.1. Study Area

The study area is located in Gongjue County, on the southeastern margin of the Tibetan Plateau along the Jinsha River (Figure 1a). Maximum elevation difference in this region is 2800 m, with an average elevation of about 3950 m. The NS Jinsha River flows through this region and converges with the Yangtze River [27]. This region belongs to a subtropical climate with annual precipitation of 500–800 mm, which has uneven distribution throughout the year. The monthly precipitation peaks in the summer months when the average rainfall is about 100 mm. The study area is characterized by strong erosion by the Jinsha River and concentrated rainfall, which is very likely to trigger landslides in the rainy season [10].

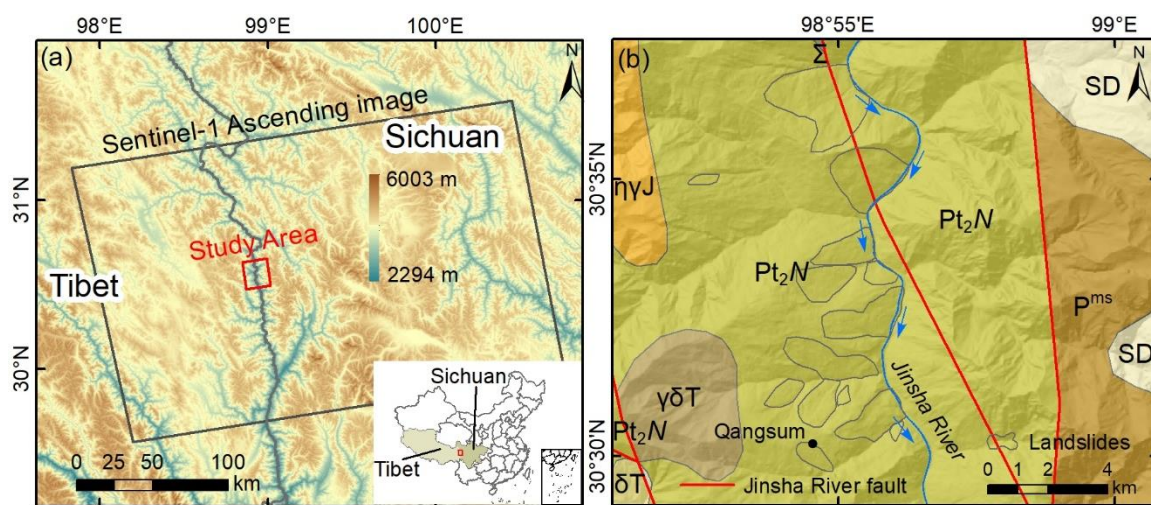


**Figure 1.** (a) Location of the study area and coverage of the SAR datasets; (b) tectonic and geological map.

Geologically, the study area mainly exposes Paleo-Mesoproterozoic strata (Figure 1b). The lithology is dominated by mica-quartzose schist and gneiss. The NNW Jinsha River fault trends across the study area, showing signs of recent tectonic activity. Under the influence of tectonic movements, steep terrain, and hydrological conditions, a fragile geological environment creates many local geological disasters. For example, in late 2018 (11 October and 3 November 2018), the Baige landslides occurred successively in Boro Town, Tibet, China, which caused upstream inundation and downstream flooding [28–30]. The Temi ancient landslide blocked the Jinsha River (about 1.8 ka BP) [1]. Therefore, the study area has a high susceptibility to geological hazards. With the continuously expansion of human activities and the deterioration of the geological environment, geological hazards in Gongjue County show an increasing trend, and the resurrection of multiple giant ancient landslides poses a major threat to the lives, property and security of residents.

### 2.2. Datasets

Time-series InSAR process along the line-of-sight (LOS) was calculated based on 119 Sentinel-1 ascending SAR images acquired from October 2017 to December 2021 (Figure 1 and Table 1). Elevation data with a resolution of 30 m acquired from the USGS were used to remove the terrain phase during the InSAR process. GAMMA software was used for the IPTA (interferometric point target analysis) process, which is a kind of PS-InSAR (permanent scatterer InSAR) technique, and the SARscape software was used to perform SBAS-InSAR in this study; detailed principles and procedures are provided in Section 3. The available maps and data layers required for the geological analysis were

prepared, including landslides, geological maps and topographical maps. A total of 10 UAV images covering all the landslides in the study area help verify the landslide information; the range of UAV images with a resolution of 0.5 m is shown in Figure 2. Four optical images were collected to observe the changes in landslides and daily time-series rainfall data with a 10 km resolution were obtained from NASA.

**Table 1.** Datasets used in this study.

Data	Resolution	Date	Number	Source
Sentinel-1	Range 2.3 m, azimuth 14 m	8 October 2017–22 December 2021	119	<a href="https://search.asf.alaska.edu">https://search.asf.alaska.edu</a> accessed on 1 January 2022
Elevation	30 m	-	1	United States Geological Survey SRTM accessed on 1 January 2022
UAV images	cm	1 May 2021–1 June 2021	10	-
Precipitation	10 km	1 October 2017–22 December 2021	daily	NASA. <a href="https://pmm.nasa.gov">https://pmm.nasa.gov</a> accessed on 2 January 2022
Sentinel-2	10 m	1 October 2016\1 March 2020	2	<a href="https://search.asf.alaska.edu">https://search.asf.alaska.edu</a> accessed on 2 January 2022
Landsat 8	15 m	1 February 2013/1 February 2019	2	<a href="https://earthexplorer.usgs.gov">https://earthexplorer.usgs.gov</a> accessed on 3 January 2022

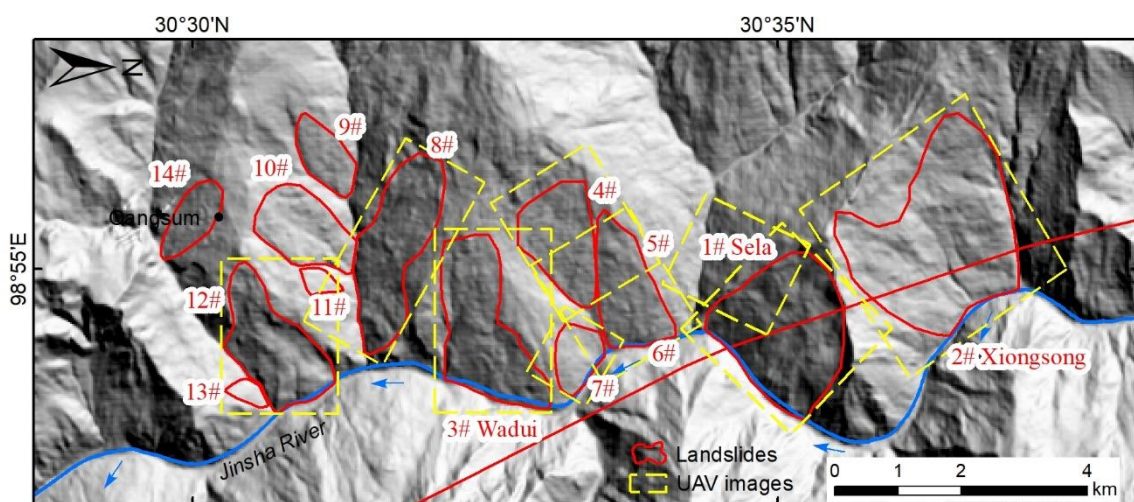


**Figure 2.** Areas covered by UAV images. Different numbers labeled the landslide.

### 3. Method

Figure 3 shows the workflow of this study. We applied two time-series InSAR methods (SBAS and PS-InSAR) for the displacement calculation. A cross-comparison between their results was conducted to verify the reliability, and the deformation areas were further verified by UAV images and field investigation. The cross-comparison approach consists mainly of complementary spatial time-series interferometric points and the comparative analysis of temporal deformation sequences. By coupling the interferometric points obtained from the two time-series InSAR methods noted above, the spatial density of the interferometric points is increased and the deformation characteristics can become more refined. The comparative analysis of deformation sequences is used to determine the reliability of the results by comparing the temporal deformation of neighboring interference points and analyzing whether the deformation magnitudes and trends are consistent. The deformation characteristics of two giant landslides were analyzed emphatically. Detailed principles and processes are introduced in the following three sections.

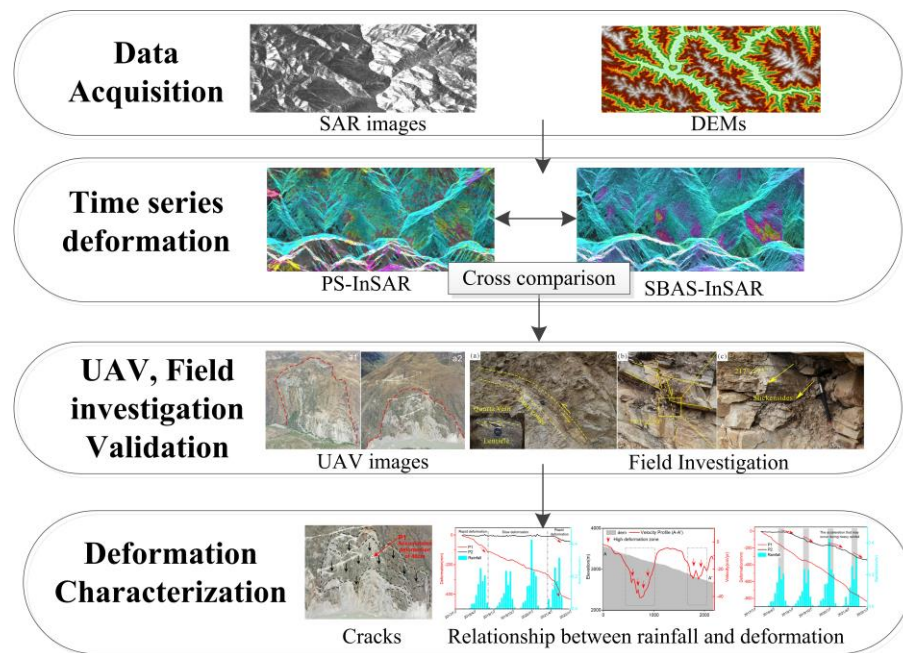


Figure 3. Workflow chart of this study.

### 3.1. SBAS-InSAR

SBAS technology can better overcome the effects of spatiotemporal decoherence and extract useful information based on multitemporal images [19]. The principle of this method is to use the coherence of spatial distribution to restore the time-series deformation by connecting multiple interferogram pairs with short spatial–temporal baselines. In this paper, 119 Sentinel-1 SAR images were processed, and the detailed parameters are shown in Table 1. Precise orbit files were downloaded and preprocessed to reduce orbital errors. To improve computational efficiency, SAR images were cropped to the study area.

The SBAS process follows (Figure 4a):

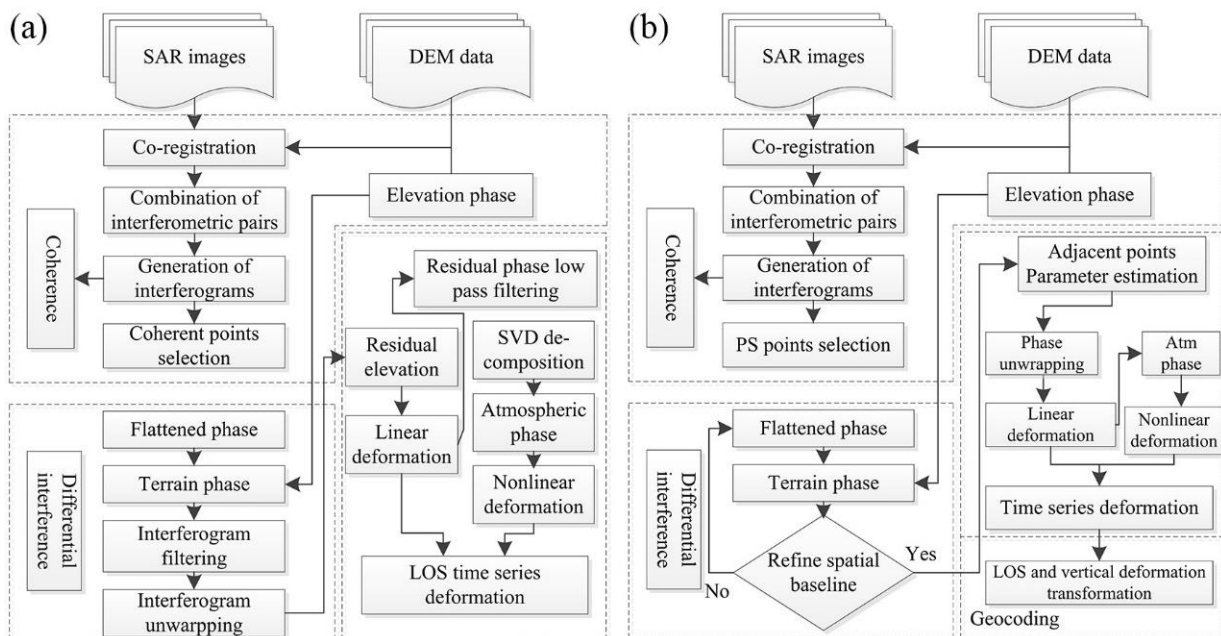
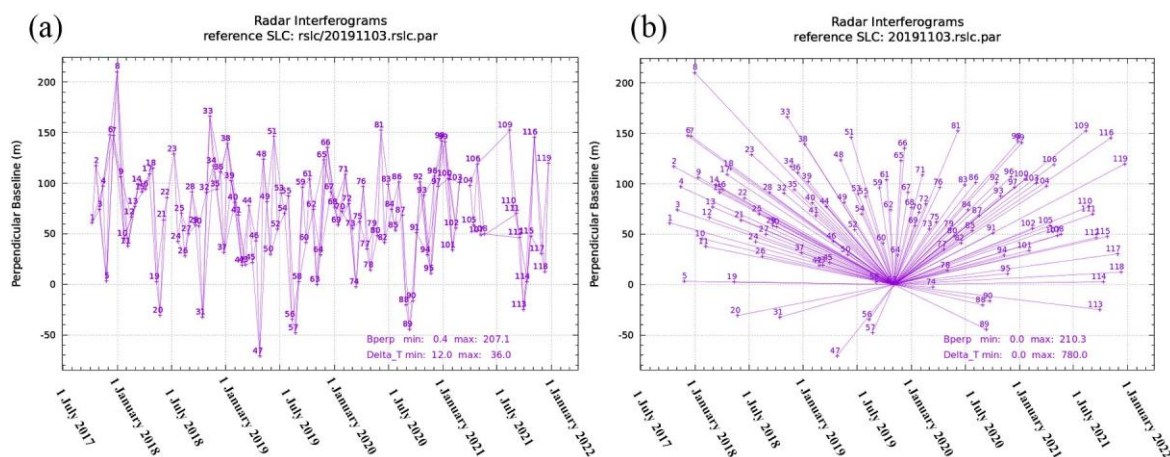


Figure 4. Workflow of (a) SBAS-InSAR and (b) PS-InSAR.

(1) The generation of differential interferograms: Temporal and spatial baselines were set at 36 days and 250 m (Figure 5a), respectively. Multilooks of the SBAS process were set to 10:2, and all possible interferogram pairs interfere after co-registration.



**Figure 5.** The spatiotemporal baselines of (a) SBASInSAR and (b) PSInSAR.

(2) Phase unwrapping: An adaptive filtering function was used to smooth the interference phase [31], and the minimum cost flow (MCF) algorithm was used to unwrap the filtered interference phase. Elevation data acquired from the USGS was used to remove the topographic phase.

(3) Inversion of deformation rate: Estimate the elevation error based on the unwrapped phase, and remove the atmospheric error by spatial filtering and temporal high-pass filtering; select high-quality distributed scatterers, and the deformation rates and time-series deformation through the singular value decomposition (SVD).

### 3.2. PS-InSAR

PS-InSAR technology is usually implemented by computing differential interferograms of all the acquisitions with respect to the same reference image [15]. Based on time-series intensity and phase information, PS-InSAR selects relatively stable scattering points for deformation analysis without multilooks processing, which can maintain high coherence for a long time. The function relation between deformation and phase difference is established by PS points, and the topographic and atmospheric errors are removed by external data or related filtering methods, so the surface deformation information on PS points can be obtained.

The processing procedure includes the following three steps (Figure 4b):

(1) Initial selection of the PS points and baselines: According to the spectral and backscattering intensity of SAR images, the permanent scatterer points were selected using thresholds of 0.7 and 2.1, respectively [15,20]. A total of 48,069 high quality PS points were selected for subsequent deformation analysis. The temporal and spatial baselines are shown in Figure 5b.

(2) Estimation of velocity and DEM errors: The stable village area was selected as the reference point, and the deformation regression analysis based on relative phase observations between nearby PS was carried out with the coherence of 0.7 as the threshold. The elevation error was estimated and corrected by three iterations of regression analysis.

(3) Time-series deformation: The atmospheric phase was removed by applying time-domain and spatial filtering techniques, and the time-series deformation phase and displacement velocity were finally calculated.

### 3.3. Validation and Deformation Characteristics Analysis

In this paper, we used the DJI M300 RTK UAV for aerial data collection, which has a longer endurance than other small UAVs. It carries a PTZ (pan tile zoom) camera with a CMOS-based sensor (20 megapixel). Pix4D is professional UAV data processing software, which we used to plan the flight route and process the aerial data. In terms of flight parameter setting, forward overlap and lateral overlap were set to 85% and 80%, respectively. Depending on the terrain conditions of the landslides, the relative flight altitude was set to 100–200 m to obtain cm ground resolution images. In addition to recording the location and elevation data of the UAV ground station, at least eight residential corners were selected as ground control points (GCPs) in each aerial photography mission, and the spatial location and elevation data of the GCPs were recorded using Trimble GPS to ensure the accuracy of the results. Finally, the aerial images were stitched and calibrated using the ground station and GCP data.

In terms of deformation characteristics analysis, we used the traditional geological survey method to verify the ground failure characteristics. The elevation difference in the DEM obtained by SRTM and UAV and multisource remote sensing data were used to verify the vertical and horizontal deformation of landslides. COSI-Corr is change detection software based on optical images, which can identify the horizontal changes in two images with long time intervals [32]. Origin and MATLAB software were used to analyze the correlation between landslide deformation information and rainfall.

## 4. Results

### 4.1. Detection and Identification of Active Landslides

Figure 6 shows the average deformation velocity along the LOS in the study area acquired by SBAS and PS-InSAR from October 2017 to December 2021. A total of 14 active landslides are densely distributed within an area of 90 km<sup>2</sup>, and their continuous deformation was completely detected. Combined, all of the detected landslides cover a total area of about 20 km<sup>2</sup>. The spatial distribution characteristics show that the landslide in the study area is mostly distributed on the right bank of Jinsha River, moving toward the WE direction. Therefore, the ascending orbit Sentinel-1 SAR images can effectively detect the movement on the east-facing slopes [9,10]. According to the final deformation rate results, although the density and distribution of deformation points in the landslide area are different, there are few differences between the deformation rates obtained by the two time-series methods. In the study area, largest deformation rate in the landslide area was more than +50 mm/y and the maximum deformation rate reached −240 mm/y, indicating that these landslides are in the slow creep stage. A detailed comparison of the rates obtained by the two methods is discussed in Section 5.

### 4.2. Validation of UAV Images and Field Investigation

InSAR deformation results can effectively show the location of the deformation zone. However, the accuracy of the deformation information needs to be verified by remote sensing images and field investigation. Most landslides in the study area are located along the Jinsha River, and the high and steep slopes and complex terrain conditions make it challenging to verify these landslides. As a countermeasure, we employed optical remote sensing and UAV images to show morphological and microtopographic features of the landslide, and verified the deformation results through field investigation. Combining morphological and microtopography features (fissures, color tones and terrain form), we identified and verified the landslide boundaries. Figure 7 shows the deformation rate and UAV images of two typical landslides. The deformation areas of the landslides corresponded well with the failure areas in the UAV images. Moreover, we observed the large deformation and failure characteristics of landslides through UAV and remote sensing images, such as rock fragmentation, fracture development and multistage dislocation (Figure 8). These failure regions are consistent with the location of large deformation regions obtained by InSAR methods.

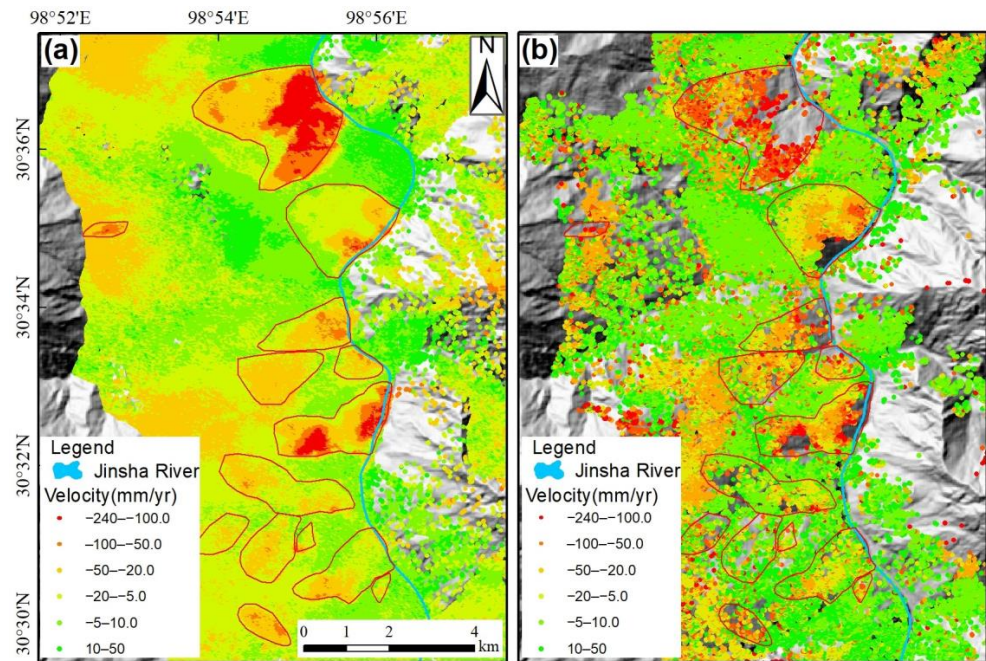


**Figure 6.** The deformation velocity of the study area was obtained by SBAS (a) and PS-InSAR (b) methods. Landslide areas are marked with red polygons. (A negative value implies moving away from the satellite; a positive value indicates moving toward the satellite along with the LOS direction).

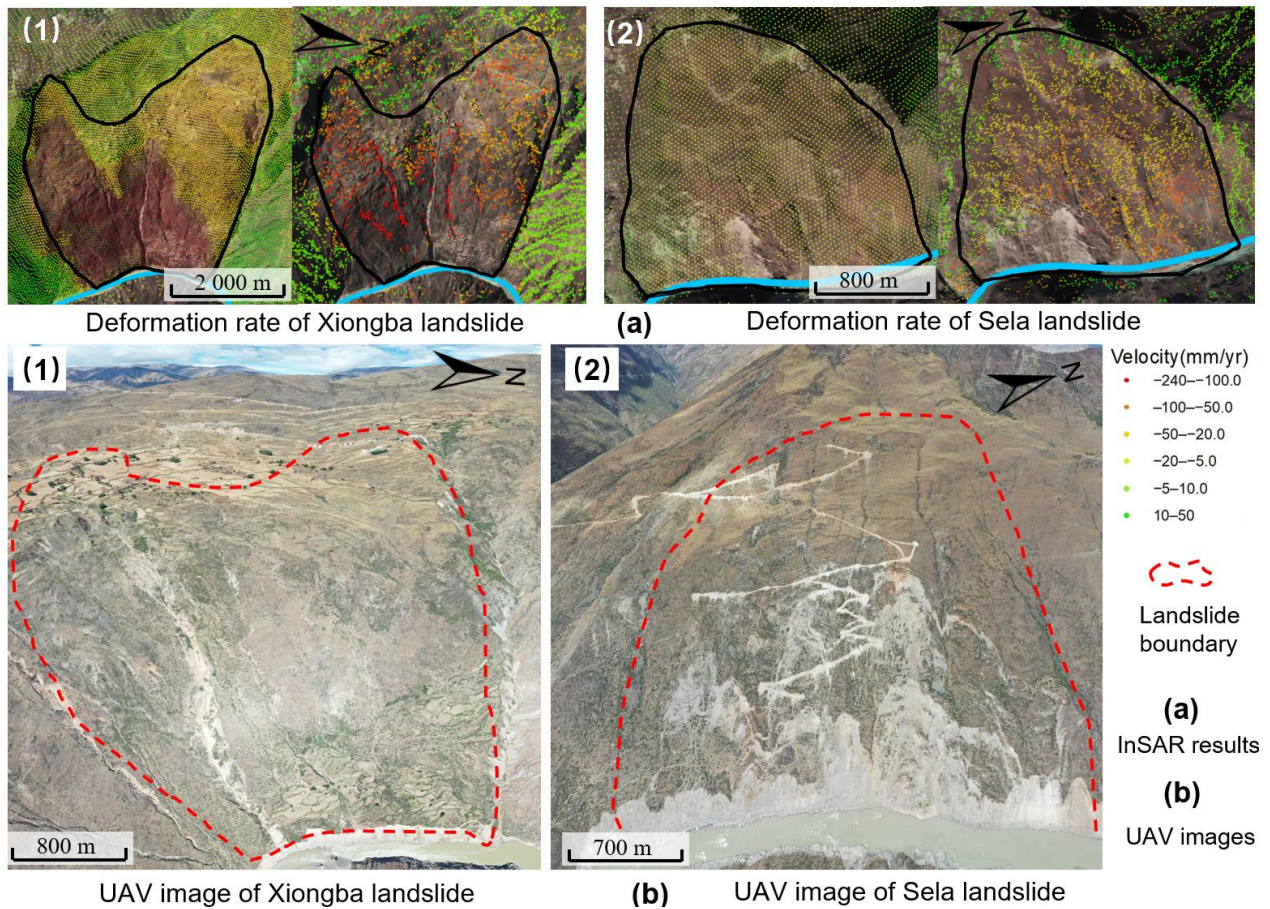


**Figure 7.** SBAS-InSAR and PS-InSAR deformation rate (a) and UAV images (b) of two typical active landslides. The red and black line in the figure represents the landslide boundary.

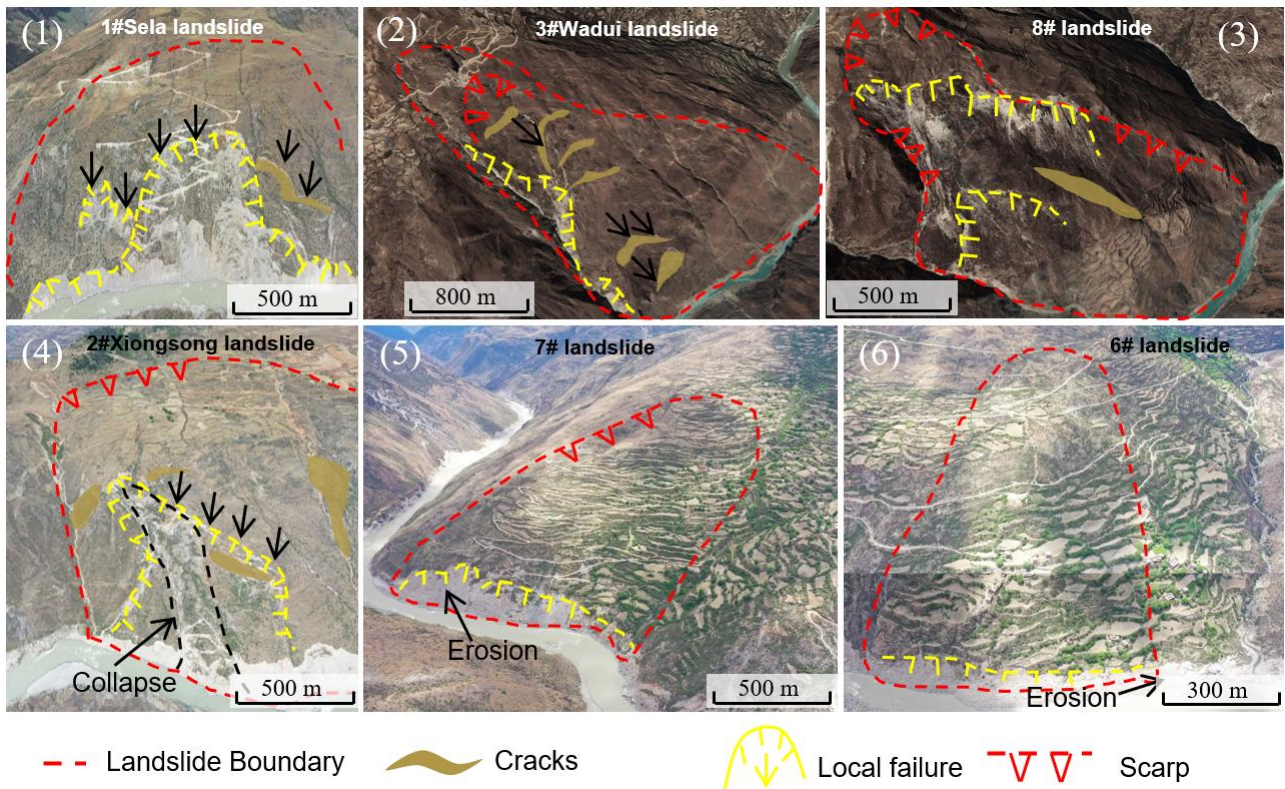


Figure 8. Fracture and local failure characteristics of landslides.

In addition, the elevation difference between SRTM and UAV-based DEM was used to qualitatively validate the vertical deformation characteristics of landslides (Figure 8). Since the SRTM DEM data were acquired in 2000, the elevation difference cannot be quantitatively compared with the temporal deformation information from the past five years (Figure 9). However, the spatial distribution of elevation differences shows that the elevation changes in the landslide area are significantly greater and are likely to be the result of long-term deformation of the landslide by gravity. The maximum cumulative elevation difference in the landslide area is 6 m, and the maximum annual settlement is about 30 cm/y, which is roughly the same as the result obtained by the time-series InSAR method.

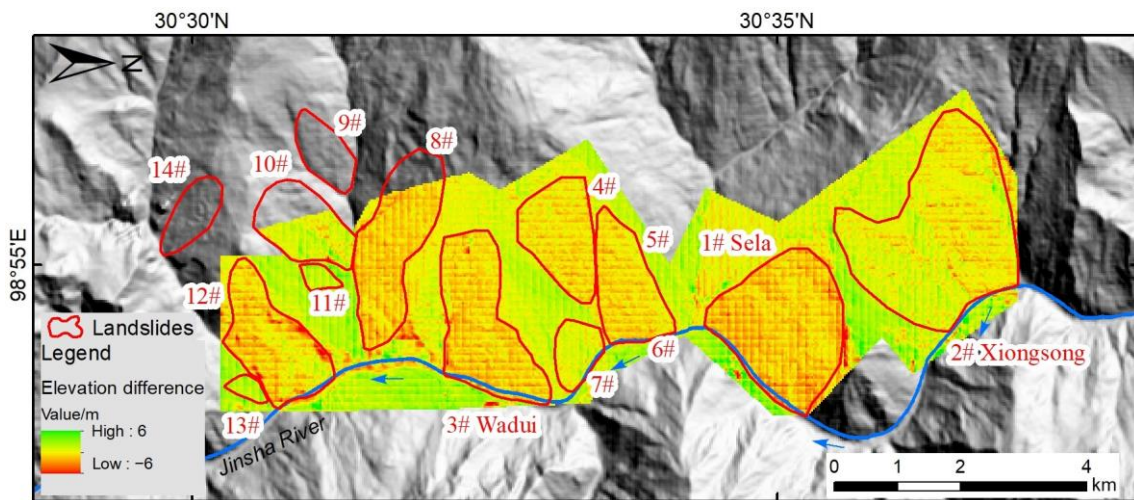
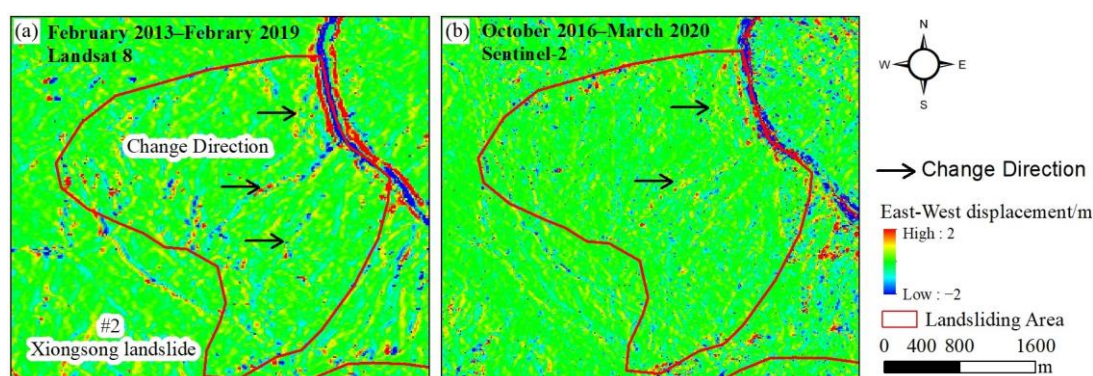


Figure 9. The elevation difference between SRTM DEM and DSM obtained from UAV images. Different numbers labeled the landslide.

The Xionsong landslide was taken as an example for change detection, and the changes detected by the COSI-Corr method based on four optical images are shown in Figure 10. Only deformations in the east–west direction were calculated because it is the main movement direction. The results show that the movement of the landslide caused spectral changes; red or blue indicates continuous tensile cracks at the scarp, and the position of the red–blue change area is consistent with the position of the rapid deformation area in Figure 7(a1,b1).



**Figure 10.** Changes in the Xionsong landslide revealed by COSI-Corr method. The red and blue regions represent the eastward and westward movement. (a) Changes detected using Landsat 8 images; (b) Changes detected using Sentinel-2 images.

#### 4.3. Deformation Characteristics of Two Giant Landslides

The deformation of two giant landslides (Sela landslide and Wadui landslide) was analyzed, which are potential landslides that can block the Jinsha River and destroy nearby villages. Both landslides are distributed on the left bank of the Jinsha River, and time-series deformation monitoring can effectively help analyze the development characteristics and influencing factors of landslides. Figure 11 shows the Sela landslide in Gongjue County, which is about 1.9 km long and 1.7 km wide, covering an area of about 2.9 km<sup>2</sup>. The average slope is about 30 degrees, and the elevation difference is 1 km. The maximum deformation area of the landslide is at the front edge, and the deformation reaches  $-240$  mm/y (Figure 11(1)). Moreover, there is relatively slow deformation on the back and middle sides of the landslide with an average deformation rate of  $-70$  mm/y. The Sela landslide belongs to retrogressive landslide, the thickness of the sliding body is about 50 m; the lower part of the landslide slides faster under river erosion. Figure 11(3,4) show enlarged images derived from UAV for the large deformation area. The collapse areas shown by the UAV images agree well with the deformation area; they are the severely deformed area at the front edge of the landslide with an area of about 0.5 km<sup>2</sup>. The exposed bedrock is visible in this area, and the broken rock mass has clear traces of tension cracks (black dotted lines) caused by material movement. Some loose debris above remains in the most unstable region, and the black arrows show the direction of movement of the broken rock mass.

Two points (P1 and P2) marked in Figure 11(1) were selected for correlation deformation analysis, and the rainfall data came from NASA. According to the rainfall data recorded at the landslide, the peak period of rainfall is from June to September, accounting for 60% of the whole year. Time-series displacement was found to be related to concentrated rainfall; landslide deformation was significantly accelerated during the rainy seasons of 2018 and 2021 (marked in red arrows), while the deformation rate remained stable during the rest of the period. However, the landslide did not show a significant acceleration of deformation between January 2019 and March 2021. Moreover, there was no significant acceleration even during heavy rainfall in August 2020, which indicated that rainfall conditions were probably not the only factor influencing the failure of the Sela landslide.

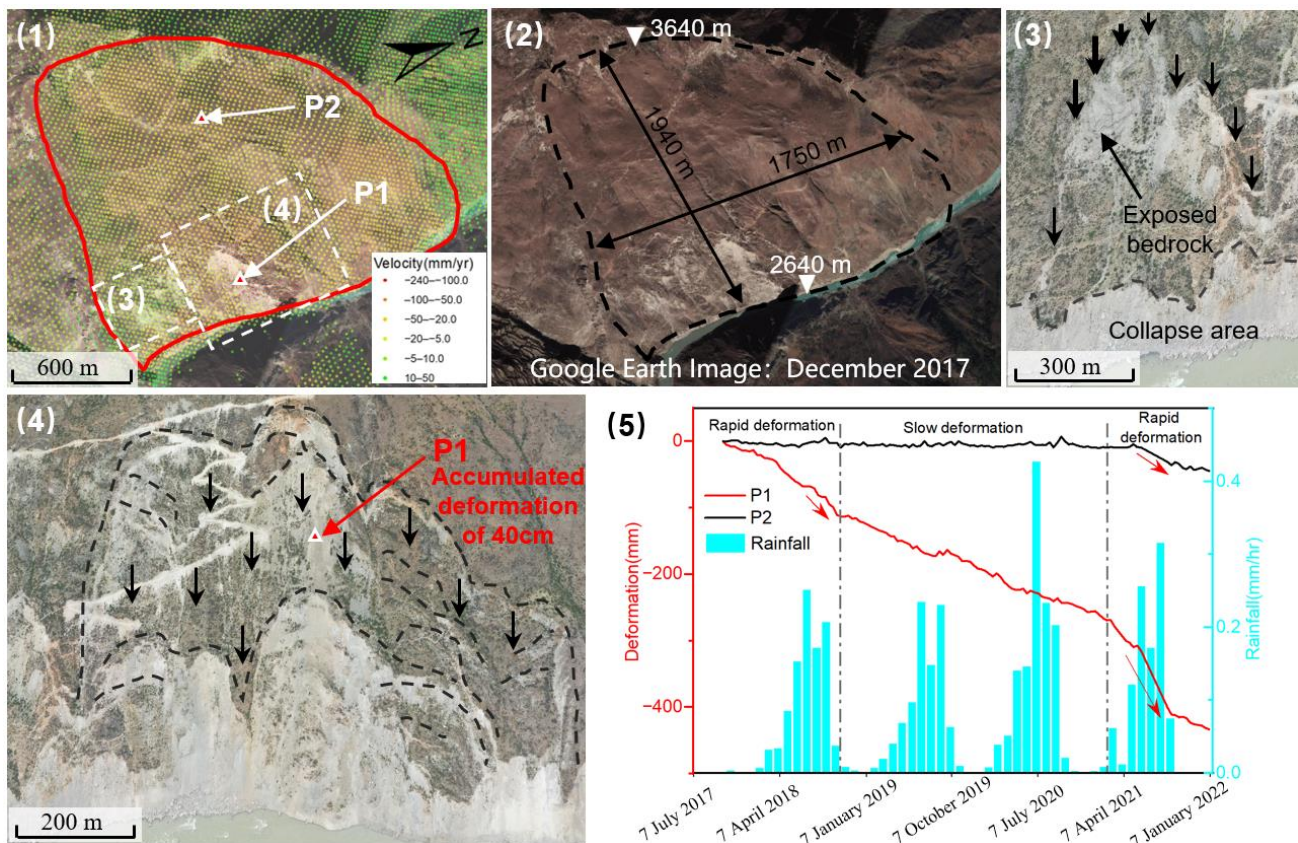


**Figure 11.** The Sela landslide in Gongjue County and its deformation characteristics: (1) average velocity of the landslide acquired from SBAS-InSAR; (2) Google Earth image; (3) local collapse at the toe of the landslide; (4) front part of the landslide has the largest deformation and has already begun to fail (black arrows indicate the direction of movement); (5) relationship between monthly precipitation and points P1 and P2 time-series deformation. The black arrows in the figures represent the direction of movement.

As shown in Figure 12, the Wadui landslide is another landslide with large deformation, which is located downstream from the Sela landslide and has an area of about 2.5 km<sup>2</sup>. Two large deformation regions are located at altitudes of 2800 and 3260 m, with maximum annual average deformation rates of  $-30$  and  $-40$  cm/y, respectively. Specifically, Figure 12(2) shows fractures caused by tensile stress and gravity on the edge of the landslide, which is about 2–5 m wide and 10–20 m deep. These fractures and some small eroded grooves resulting from rain wash on the surface are visible in the Google Earth image, and this area is the most damaged at the Wadui landslide. We plotted the deformation rate profile (A–A') along the slope, which more intuitively shows the settlement rates of the two large deformation zones in the landslide. The deformation profile shows that the deformation in the middle part of the landslide was small. In contrast, the deformation in the front and rear was large, which indicates that the landslide is a discontinuous deformation. The Wadui landslide is a shallow landslide with a thickness of about 25 m, and is susceptible to slippage due to rainfall. We selected two deformation feature points (P1 and P2 in Figure 12(1)) in two large deformation regions and analyzed their correlation by combining the time-series deformation and rainfall data (Figure 12(4)). Two feature points exhibit distinct responses to rainfall; the cumulative deformation of point P1 in the past five years has reached 80 cm, located in the most rapidly damaged area. Nevertheless, its deformation rate did not change greatly, and there is no obvious relationship to the change in rainfall conditions. In contrast, Point P2, located on the front edge of the landslide, showed a strong response to rainfall. In the annual rainy season (June–August),

Point P2 has an obvious accelerated deformation phenomenon (red arrow), and the time of accelerated deformation also has a significant lag relationship with the time of heavy rainfall. The time-series curves of the two points show that the landslide has been affected by different factors in multiple areas, which induces a series of deformation phenomena.

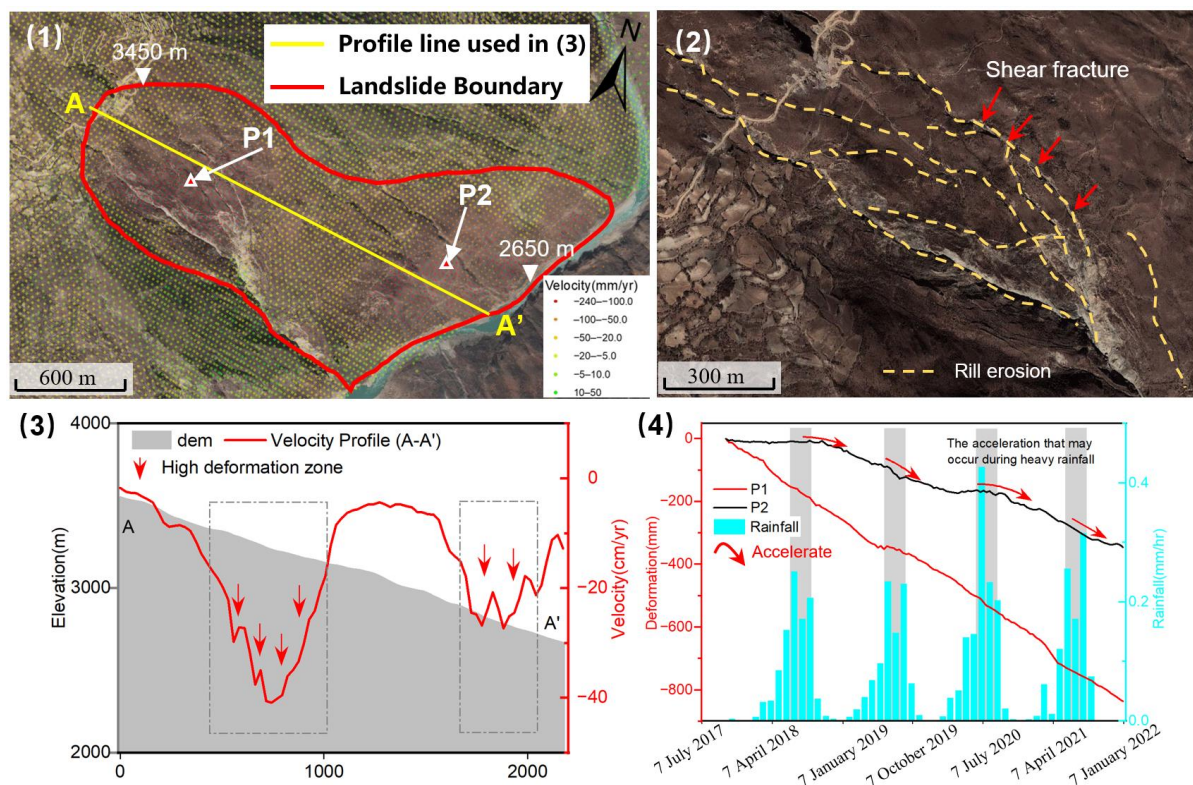


**Figure 12.** The Wadui landslide in Gongjue County and its deformation characteristics: (1) average velocity of the landslide acquired from SBAS-InSAR; (2) local Google Earth image; (3) deformation profile along A-A' in (1) shows two large deformation regions; (4) relationship between monthly precipitation and points P1 and P2 time-series deformation.

## 5. Discussion

### 5.1. Comparison between SBAS and PS-InSAR

SBAS and PS-InSAR were cross-compared to prove the accuracy and precision of deformation results. We compared these two methods from three aspects: scatterer point density, deformation rate distribution and time-series deformation. Figure 13 shows the spatial distribution range of time-series points and the histogram of deformation rate distribution. The zoom-in subsets of two landslides shown in Figure 13b–e reveal that compared with PS-InSAR, the SBAS method can obtain more time-series deformation points. For the SBAS method, a total of 28,964 time-series points within the landslide area of 12 km<sup>2</sup> with a density of 2400 points/km<sup>2</sup>, while the PS-InSAR method only extracted 16,124 valid permanent scatterer points. Owing to the spatial multilook process in the SBAS method, relatively uniform time-series points (Figure 13b,d) can be obtained, which have good coverage for deformation calculation in the whole landslide region. However, this method sacrifices pixel resolution and it is easy to lose high-quality scatterer signals. The PS method performs time-series deformation analysis on the highly time-coherent and stable strong reflector information at the pixel resolution. However, in the region of large gradient deformation, PS points are rare, and it is difficult to capture much deformation information (Figure 13c,e). Figure 13f,g plots two histograms of the annual deformation velocity (positive and negative values represent the surface movement toward and away from the SAR satellite, respectively), indicating a normal distribution with the average deformation

values of  $-37.33$  and  $-33.70$  mm/y, respectively. Moreover, the median values of the deformation rate obtained by the two methods are  $-25.649$  and  $18.886$  mm/y, respectively, which indicate that these two methods have consistency in the spatial distribution of the deformation rate.

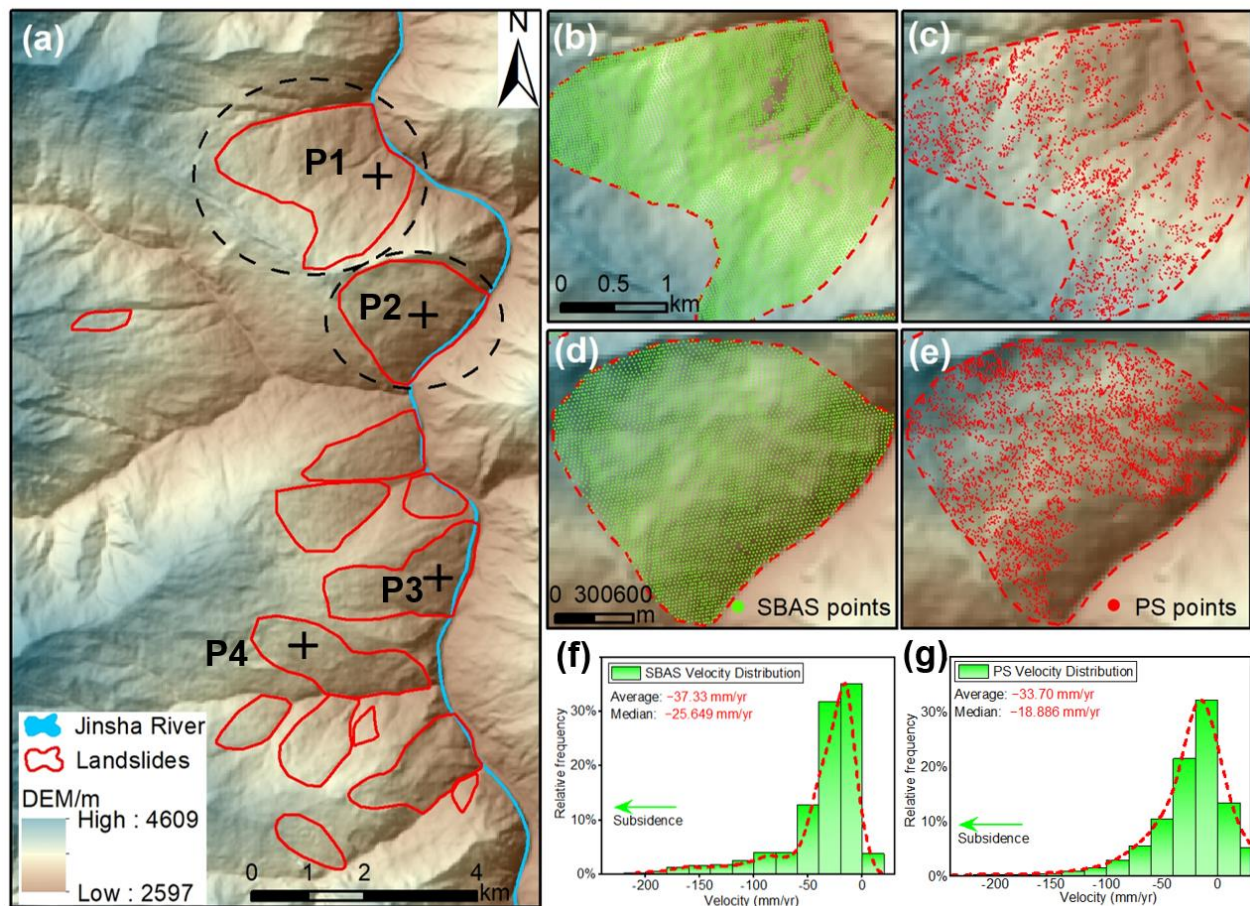


**Figure 13.** Time-series points distribution and histogram of deformation rate of SBAS and PS-InSAR: (a) spatial position of landslides; (b–e) time-series points of two large landslides; (f,g) histogram of deformation rate, the normal density function is fit by red dotted lines.

To test the accuracy of deformation results under different time-series methods, four feature points (black cross curve in Figure 13a) were selected for comparative analysis; the distance between comparison points of PS and SBAS is less than 10 m. Figure 14 shows the time-series deformation of the four feature points. In general, the overall deformation trend of SBAS and PS-InSAR results is consistent, and the deformation rate of feature points increases gradually during the four years. Although their cumulative deformation and velocity are roughly the same, the deformation curves of PS-InSAR results are more discrete than those of SBAS, and SBAS results are more stable and conform to the linear deformation model (Figure 14). Discrete deformation points of the PS-InSAR method are probably from the long-time baseline. This deformation error is common in PS-InSAR processing [18], but it is difficult to reduce effectively. However, the SBAS method uses short-time and spatial baseline interferogram pairs, which can effectively reduce deformation errors and help analyze the correlation between time-series deformation and external factors.

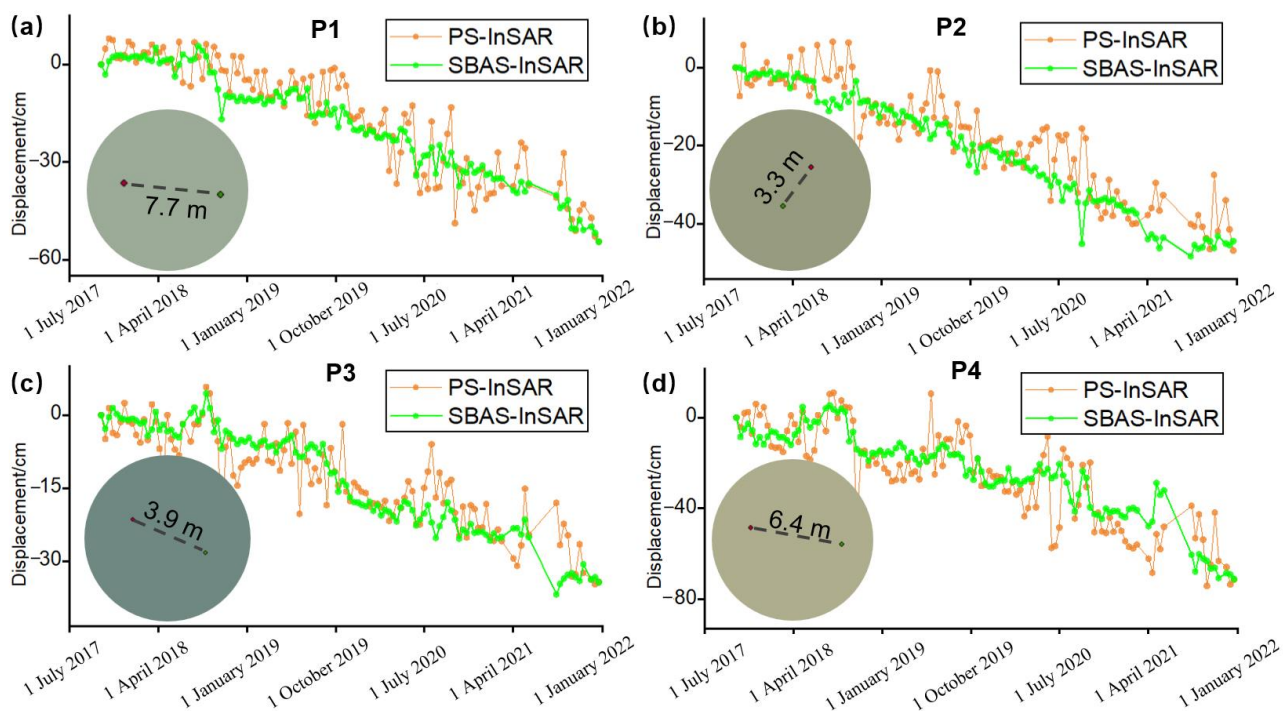


**Figure 14.** Comparison between SBAS and PS-InSAR deformation in the LOS direction at four larger deformation points. (a–d) show the displacement data of four points marked in Figure 13a. Red and green lines indicate the PS-InSAR and SBAS deformation time-series, respectively. The relative spatial positions of PS and SBAS points are shown in the circle diagram.

In some studies, ascending and descending SAR images were utilized to compare and verify the surface deformation results, and the three-dimensional deformation field can be retrieved from multiple observation measurements [9,10]. However, this method is not applicable in this study area—most of the landslides studied are oriented to the east, and the observation direction of descending images is nearly perpendicular to the direction of movement of the landslides, making it difficult to effectively observe the deformation of the landslides (Figure 15b). Therefore, this method was not used for the comparative analysis and validation of the deformation results.

### 5.2. Influence of Quaternary Tectonic Activity on Landslides

Many scholars have analyzed the relationship between the development characteristics of landslides, topography and rainfall factors [9]. However, the landslide hazard developed in the study area is not only related to the high and steep terrain, rainfall and river erosion, it is also easily affected by fault movement. Landslides in the study area are located in the Jinsha River suture zone, and the tectonic activity affects the structural evolution of the slope, which is an important factor for landslide development. Under the influence of multistage tectonic movement, slope joints and fissures develop, weathering and water events accelerate the evolution of slope structure, increasing the degree of rock fragmentation and reducing the mechanical strength of rock. Several NNS direction faults (Xionsong–Suwalong fault) and dense small faults [33] are distributed in the study area. These faults are located near the landslide or directly pass through the landslide body, causing changes in the stress field within the slope and reducing slope stability.

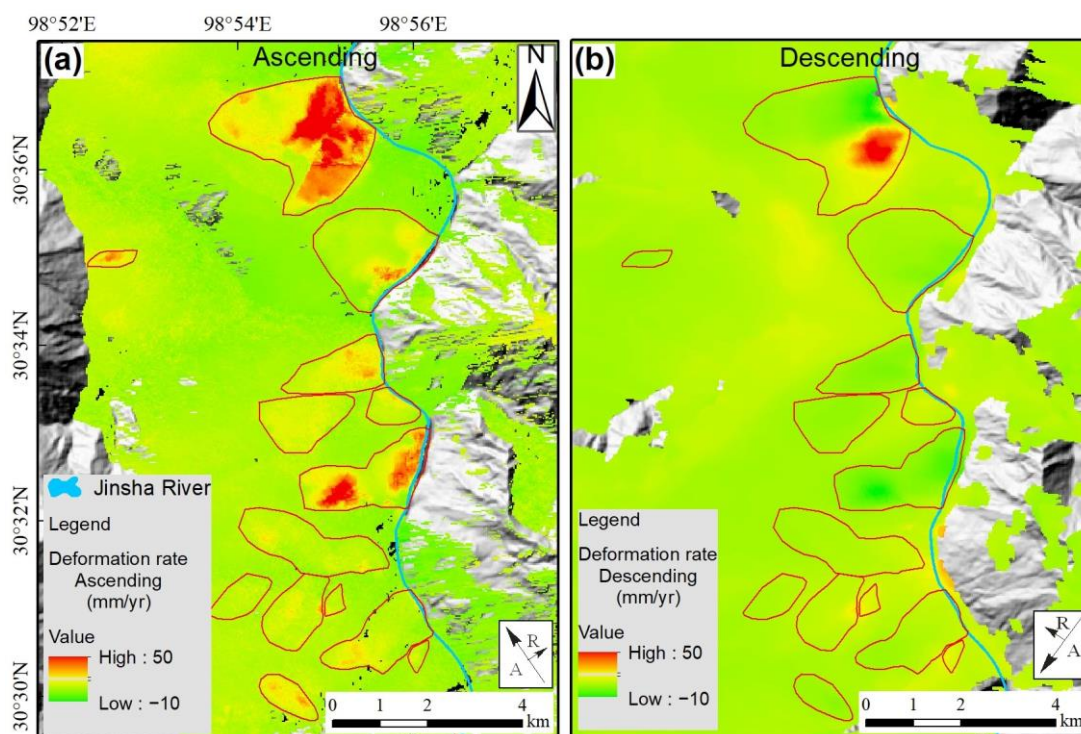


**Figure 15.** Comparison of deformation results in the ascending and descending measurement directions. (a) LOS deformation acquired from Sentinel-1 ascending images; (b) LOS deformation acquired from Sentinel-1 descending images.

The Xionsong–Suwalong reverse fault (Figure 16 (F1 and F2)) crosses through the middle and rear part of the Xionsong landslide, which may be one of the inducing factors for the large deformation. Therefore, we take the Xionsong landslide as an example to analyze the influence of fault-zone activity on the development of landslides. The engineering geological map of the Xionsong landslide is shown in Figure 16. Two NNS reverse faults (F1 and F2) cross the middle and rear of the landslide [33], which are branch faults of the Jinsha River fault. Influenced by the Jinsha River fault, there has been strong tectonic activity since the Early–Middle Pleistocene.

We carried out the field investigation near the fault zone and found that the development characteristics of reverse faults are obvious. Figure 17 shows four outcrops with reverse faults and geological engineering profiles of the Xionsong landslide (the positions of outcrops are marked in Figure 16 (P1–P4)). Figure 17a shows a quartz vein under the fault dislocation, with a dislocation distance of about 15 cm. Figure 17b,c shows two reverse faults; the upper wall of the faults clearly shows the directional compression deformation of quartz schist under the compression environment. The S-shaped quartz vein also indicates a complex stress environment within the slope (Figure 17d). Figure 17 shows the geological profile of the Xionsong landslide; the slope is dominated by gneiss and quartz schist, and its occurrence is about  $250^{\circ}\sim 260^{\circ}\angle 10^{\circ}\sim 20^{\circ}$ , which is a reverse slope. Literature and drilling data [33,34] indicate that the potential slip-surface of the Xionsong landslide is located in the vicinity of the F1 fault, which extends from the depth of the slope to the surface. Through detailed ground geological investigations, we have found many signs of fault activity, large and small, which are directly observable at the surface. This suggests that the active faults in the landslide area have created a stress–extrusion environment beneath the landslide. The rock mass is more susceptible to breakage by gravitational compression, reducing slope stability. Long-term fracture activity contributes to the development of landslides.

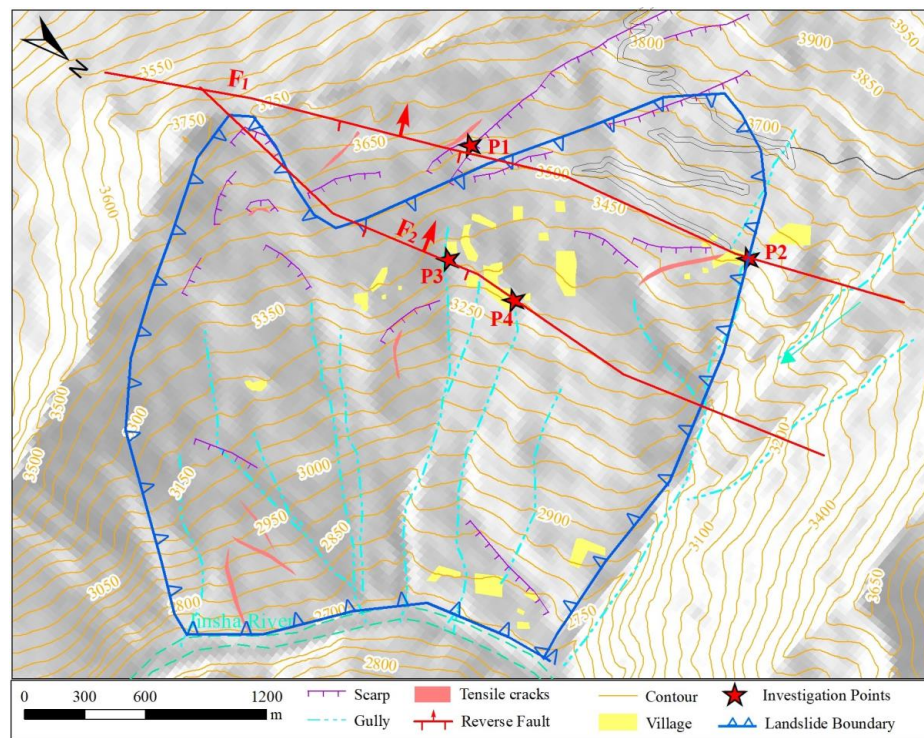


**Figure 16.** The reverse faults (F1 and F2 marked in red lines) cross the Xionsong landslide (fault and landslide data from references [10,33]).

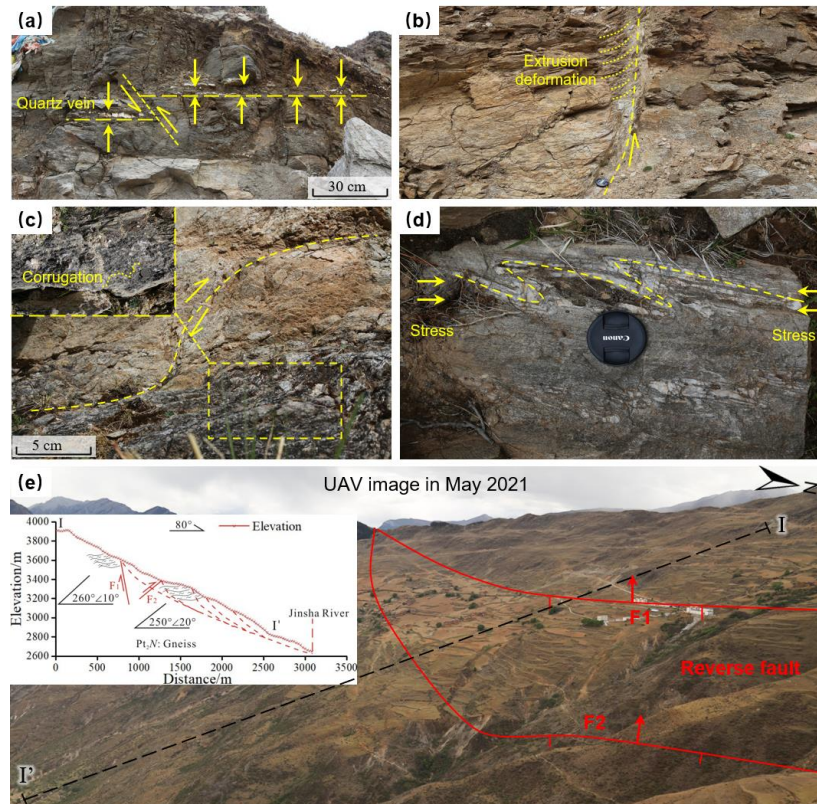


**Figure 17.** Characteristics of surface fault activity within the Xionsong landslide. Locations of features (a–d) are shown as points in Figure 16 (P1–P4). (e) shows the UAV image and geological profile of the landslide.

## 6. Conclusions

InSAR technology has been widely used in landslide identification, but the single deformation observation method may have great uncertainty, resulting in wrong judgment during the process of landslide detection [24,35]. Effective verification methods are significant to disaster identification, risk assessment and mechanism analysis [36–38]. Therefore, in this study, a cross-comparison method between SBAS and PS-InSAR technology was applied to identify landslides comprehensively, and UAV images and field investigation were used to validate the deformation characteristics of InSAR. Many ancient landslides are distributed along the Jinsha River in Gongjue County, so we conducted the deformation characteristics research in this area and obtained the following conclusions.

(1) Both PS and SBAS methods can effectively provide deformation information for landslides in the study area. A total of 14 landslides were identified by using two kinds of time-series InSAR technology. Comparative analysis shows that the deformation results obtained by the two time-series methods are consistent in terms of cumulative deformation and deformation trend. However, the PS method can give relatively little deformation information in the large deformation area. In contrast, the SBAS method can provide more comprehensive signal coverage because of the shorter time and space baseline.

(2) UAV images and field investigation results validate the accuracy of InSAR in identifying landslides. Elevation data and the COSI-Corr method based on multisource remote sensing data were used to verify the horizontal and vertical deformation. Additionally, the severe damage areas visible on the remote image also show large deformation in InSAR results, and the damage areas in InSAR correspond well with the large deformation areas.

(3) Based on the study of two large landslides in the study area, we analyzed the correlation between landslide deformation and monthly precipitation. Results show that the deformation of the Sela landslide is related to concentrated rainfall. Deformation of the Sela landslide was significantly accelerated in the rainy season of 2018 and 2021. The Wadui landslide is located in the lower reaches of Sela landslide, and the area in front of the landslide is strongly responsive to rainfall. In the rainy season of each year, there is an obvious phenomenon of accelerated deformation, and the time of accelerated deformation and the time of heavy rainfall have a significant lag relationship.

**Author Contributions:** J.Y. conceived the manuscript; X.Y. provided funding support and helped improve the manuscript; X.L. provided relevant data. All authors have read and agreed to the published version of the manuscript.

**Funding:** The work was funded by China Three Gorges Corporation (YMJ(XLD)/(19)110), National Key R&D Program of China (2018YFC1505002), China Geology Survey Project (DD20221738-2) and the National Science Foundation of China (41672359).

**Data Availability Statement:** Sentinel-1A data used in this study were provided by European Space Agency (ESA) through the Sentinel-1 Scientific Data Hub.

**Acknowledgments:** We are very grateful for the Sentinel-1A data provided by European Space Agency (ESA).

**Conflicts of Interest:** The authors declare no conflict of interest.

## References

1. Chen, J.; Cui, Z.; Chen, R.; Zheng, X. The origin and evolution of the Temi paleolandslide-dammed lake in the upper Jinsha River. *Earth Sci. Front.* **2021**, *28*, 85–93.
2. Xu, Q.; Guo, C.; Dong, X.; Li, W.; Lu, H.; Fu, H.; Liu, X. Mapping and Characterizing Displacements of Landslides with InSAR and Airborne LiDAR Technologies: A Case Study of Danba County, Southwest China. *Remote Sens.* **2021**, *13*, 4234. [[CrossRef](#)]
3. Chen, S.; Chen, J.; Qiao, C.; Ma, J.; Liu, C. Application of Graphic and moment methods on the analysis of particle sizes of Dam-break accumulations by Xuelongnang ancient landslide lake in the Upper Jinsha River. *Geoscience* **2017**, *31*, 1278–1283.
4. Dai, K.; Tie, Y.; Xu, Q.; Ma, Y.; Zhuo, G.; Shi, X. Early identification of potential landslide geohazards in al-pine-canyon terrain based on SAR interferometry—a case study of the middle section of yalong river. *J. Radars* **2020**, *9*, 554–568.
5. Yao, X.; Li, L.; Zhang, Y.; Zhou, Z.; Liu, X. Types and characteristics of slow-moving slope geo-hazards recognized by TS-InSAR along Xianshuihe active fault in the eastern Tibet Plateau. *Nat. Hazard* **2017**, *88*, 1727–1740. [[CrossRef](#)]

6. Fan, X.; Xu, Q.; Alonso-Rodriguez, A.; Subramanian, S.; Li, W.; Zheng, G.; Dong, X.; Huang, R. Successive landsliding and damming of the Jinsha River in eastern Tibet, China: Prime investigation, early warning, and emergency response. *Landslides* **2019**, *16*, 1003–1020. [[CrossRef](#)]
7. Yao, X.; Deng, J.; Liu, X.; Zhou, Z.; Yao, J.; Dai, F.; Ren, K.; Li, L. Primary Recognition of Active Landslides and Development Rule Analysis for Pan Three-river-parallel Territory of Tibet Plateau. *Adv. Eng. Sci.* **2020**, *52*, 16–37.
8. Zhang, Y.; Meng, X.; Dijkstra, T.A.; Jordan, C.J.; Chen, G.; Zeng, R.; Novellino, A. Forecasting the magnitude of potential landslides based on InSAR techniques. *Remote Sens. Environ.* **2020**, *241*, 111738. [[CrossRef](#)]
9. Liu, X.; Zhao, C.; Zhang, Q.; Lu, Z.; Li, Z.; Yang, C.; Zhu, W.; Liu-Zeng, J.; Chen, L.; Liu, C. Integration of Sentinel-1 and ALOS/PALSAR-2 SAR datasets for mapping active landslides along the Jinsha River corridor, China. *Eng. Geol.* **2021**, *284*, 106033. [[CrossRef](#)]
10. Yao, J.; Lan, H.; Li, L.; Cao, Y.; Wu, Y.; Zhang, Y.; Zhou, C. Characteristics of a rapid landsliding area along Jinsha River revealed by multi-temporal remote sensing and its risks to Sichuan-Tibet railway. *Landslides* **2022**, *19*, 703–718. [[CrossRef](#)]
11. Eriksen, H.O.; Lauknes, T.R.; Larsen, Y.; Corner, G.D.; Bergh, S.G.; Dehls, J.; Kierulf, H.P. Visualizing and interpreting surface displacement patterns on unstable slopes using multi-geometry satellite SAR interferometry (2D InSAR). *Remote Sens. Environ.* **2017**, *191*, 297–312. [[CrossRef](#)]
12. Intrieri, E.; Carla, T.; Gigli, G. Forecasting the time of failure of landslides at slope-scale: A literature review. *Earth-Sci. Rev.* **2019**, *193*, 333–349. [[CrossRef](#)]
13. Intrieri, E.; Frodella, W.; Raspini, F.; Bardi, F.; Tofani, V. Using satellite interferometry to infer landslide sliding surface depth and geometry. *Remote Sens.* **2020**, *12*, 1462. [[CrossRef](#)]
14. Zhou, C.; Cao, Y.; Hu, X.; Yin, K.; Wang, Y.; Catani, F. Enhanced dynamic landslide hazard mapping using MT-InSAR method in the Three Gorges Reservoir Area. *Landslides* **2022**, *19*, 1585–1597.
15. Ferretti, A.; Prati, C.; Rocca, F. Permanent scatterers in SAR interferometry. *IEEE Transactions Geosci. Remote Sens.* **2001**, *39*, 8–20. [[CrossRef](#)]
16. Ferretti, A.; Fumagalli, A.; Novali, F.; Prati, C.; Rocca, F.; Rucci, A. A New Algorithm for Processing Interferometric Data-Stacks: SqueeSAR. *IEEE Transactions Geosci. Remote Sens.* **2011**, *49*, 3460–3470.
17. Berardino, P.; Fornaro, G.; Lanari, R.; Sansosti, E. A new algorithm for surface deformation monitoring based on small baseline differential SAR interferograms. *IEEE Trans. Geosci. Remote Sens.* **2002**, *40*, 2375–2383. [[CrossRef](#)]
18. Zhang, L.; Ding, X.; Lu, Z. Modeling PSInSAR Time Series Without Phase Unwrapping. *IEEE Transactions Geosci. Remote Sens.* **2011**, *49*, 547–556.
19. Hooper, A.; Bekaert, D.; Spaans, K.; Arikan, M. Recent advances in SAR interferometry time series analysis for measuring crustal deformation. *Tectonophysics* **2012**, *514*, 1–3.
20. Dun, J.; Feng, W.; Yi, X.; Zhang, G.; Wu, M. Detection and Mapping of Active landslides before Impoundment in the Baihetan Reservoir Area (China) based on the Time-Series InSAR method. *Remote Sens.* **2021**, *13*, 3213. [[CrossRef](#)]
21. Chen, F.; Zhou, W.; Tang, Y.; Li, R.; Lin, H.; Balz, T.; Luo, J.; Shi, P.; Zhu, M.; Fang, C. Remote sensing-based deformation monitoring of pagodas at the Bagan cultural heritage site, Myanmar. *Int. J. Digit. Earth* **2022**, *15*, 770–788. [[CrossRef](#)]
22. Biswas, K.; Chakravarty, D.; Mitra, P.; Misra, A. Spatial-Correlation Based Persistent Scatterer Interferometric Study for Ground Deformation. *J. Indian Soc. Remote Sens.* **2017**, *45*, 913–926. [[CrossRef](#)]
23. Xu, H.; Chen, F.; Zhou, W. A comparative case study of MTInSAR approaches for deformation monitoring of the cultural landscape of the Shanhaiguan section of the Great Wall. *Herit. Sci.* **2021**, *9*, 71. [[CrossRef](#)]
24. Bui, L.K.; Le, P.V.V.; Dao, P.D.; Nguyen, N.Q.; Pham, H.V.; Tran, H.H.; Xie, L. Recent land deformation detected by Sentinel-1A InSAR data (2016–2020) over Hanoi, Vietnam, and the relationship with groundwater level change. *GIScience Remote Sens.* **2021**, *58*, 161–179. [[CrossRef](#)]
25. Moghaddam, N.F.; Samsonov, S.V.; Rudiger, C.; Walker, J.P.; Hall, W.D.M. Multi-temporal SAR observations of the Surat Basin in Australia for deformation scenario evaluation associated with man-made interactions. *Environ. Earth Sci.* **2016**, *75*, 4. [[CrossRef](#)]
26. Lu, H.; Li, W.; Xu, Q.; Dong, X.; Dai, C.; Wang, D. Detection of Landslides in the Upstream and Downstream Areas of the Baige Landslide, the Jinsha River Based on Optical Remote Sensing and InSAR Technologies. *Geomat. Inf. Sci. Wuhan Univ.* **2019**, *44*, 1342–1354.
27. Cui, Y.; Bao, P.; Xu, C.; Fu, G.; Jiao, Q.; Luo, Y.; Shen, L.; Xu, X.; Liu, F.; Lyu, Y.; et al. A big landslide on the Jinsha River, Tibet, China: Geometric characteristics, causes, and future stability. *Nat. Hazards* **2020**, *104*, 2051–2070. [[CrossRef](#)]
28. Yang, W.; Wang, Y.; Wang, Y.; Ma, C.; Ma, Y. Retrospective deformation of the Baige landslide using optical remote sensing images. *Landslides* **2019**, *17*, 659–668. [[CrossRef](#)]
29. Li, Y.; Jiao, Q.; Hu, X.; Li, Z.; Li, B.; Zhang, J.; Jiang, W.; Luo, Y.; Li, Q.; Ba, R. Detecting the slope movement after the 2018 Baige Landslides based on ground-based and space-borne radar observations. *Int. J. Appl. Earth Obs. Geoinf.* **2020**, *84*, 101949. [[CrossRef](#)]
30. Zhang, X.; Xue, R.; Wang, M.; Yu, Z.; Li, B.; Wang, B. Field investigation and analysis on flood disasters due to Baige Landslide dam break in Jinsha River. *Adv. Eng. Sci.* **2020**, *52*, 89–100.
31. Goldstein, R.M.; Werner, C.L. Radar interferogram filtering for geophysical applications. *Geophys. Res. Lett.* **1998**, *25*, 4035–4038. [[CrossRef](#)]

32. Baird, T.; Bristow, C.; Vermeesch, P. Measuring sand dune migration rates with COSI-Corr and Landsat: Opportunities and Challenges. *Remote Sens.* **2019**, *11*, 2423. [[CrossRef](#)]
33. Yan, Y.; Guo, C.; Zhang, Y.; Zhang, X.; Zheng, Y.; Li, X.; Yang, Z.; Wu, R. Study of the deformation characteristics of the Xiongba ancient landslide based on SBAS-InSAR method, Tibet, China. *Acta Geol. Sin.* **2021**, *95*, 3556–3570.
34. Li, X.; Guo, C.; Yang, Z.; Liao, W.; Wu, R.; Jin, J.; He, Y. Development characteristics and formation mechanism of the Xiongba giant ancient landslide in the Jinshajiang Tectonic Zone. *Geoscience* **2021**, *35*, 47–55.
35. Li, F.; Liu, G.; Gong, H.; Chen, B.; Zhou, C. Assessing Land Subsidence-Inducing Factors in the Shandong Province, China, by Using PS-InSAR Measurements. *Remote Sens.* **2022**, *14*, 2875. [[CrossRef](#)]
36. Dou, J.; Yunus, A.P.; Bui, D.T.; Merghadi, A.; Sahana, M.; Zhu, Z.; Chen, C.W.; Han, Z.; Pham, B.T. Improved landslide assessment using support vector machine with bagging, boosting, and stacking ensemble machine learning framework in a mountainous watershed, Japan. *Landslides* **2020**, *17*, 641–658. [[CrossRef](#)]
37. Guzzetti, F.; Reichenbach, P.; Cardinali, M.; Galli, M.; Ardizzone, F. Probabilistic landslide hazard assessment at the basin scale. *Geomorphology* **2005**, *72*, 272–299. [[CrossRef](#)]
38. Marjanovic, M.; Kovacevic, M.; Bajat, B.; Vozenilek, V. Landslide susceptibility assessment using SVM machine learning algorithm. *Eng. Geol.* **2011**, *123*, 225–234.